Separation and Purification Technology 390 (2026) 136946

Contents lists available at ScienceDirect

Separation and Purification Technology

journal homepage: www.elsevier.com/locate/seppur

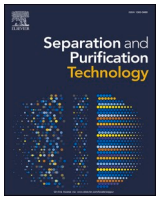

High-throughput screening of mRNA precipitate filterability using automated image analysis

Maria del Carme Pons Royo [a,*], Mateo Camara Largo [b,c], Didac Alonso Lopez [d], Soroush Ahmadi [a], Andrew Hatas [a], Allan S. Myerson [a], Richard D. Braatz [a]

[a] Department of Chemical Engineering, Massachusetts Institute of Technology, 77 Massachusetts Avenue, Cambridge, MA 02139, United States
[b] Signal Processing Applications Group. Information Processing and Telecommunications Center. Avda. Complutense 30, ETSI de Telecomunicación, Universidad Politécnica de Madrid, Spain
[c] Research Laboratory of Electronics, Massachusetts Institute of Technology, 77 Massachusetts Avenue, Cambridge, MA 02139, United States
[d] Centro de Formación Interdisciplinaria Superior – Universitat Politècnica de Catalunya (CFIS-UPC), Carrer de Pau Gargallo, 14, Les Corts, 08028 Barcelona, Spain

ARTICLE INFO

Editor Name: Raquel Aires Barros

Keywords:
Precipitation
Continuous bioprocessing
Critical flux
Packing density
Image analysis
Filterability

ABSTRACT

The integration of precipitation as a non-chromatographic, non-titer-dependent capture method has received increasing attention in continuous bioprocessing for biotherapeutics. Precipitation offers a scalable and cost-effective approach to separate biomolecules by reducing solubility through changes in pH, ionic strength, or the addition of precipitating agents. Following precipitation, efficient solid–liquid separation is required to remove formed solids from the liquid phase, a step commonly performed using tangential flow filtration. For continuous TFF operation, maintaining stable filtration performance over time is essential. A key factor is the critical flux, defined as the maximum permeate flux that can be sustained without significant membrane fouling. Previous studies, focused on monoclonal antibodies, have shown that buffer composition, salt type, and precipitant addition strategy strongly influence precipitate morphology and filterability. However, these relationships have not been evaluated for messenger RNA (mRNA). Accurate assessment of packing density is essential for predicting filtration performance; however, conventional techniques to determine the packing density suffer from limitations related to throughput, sample volume requirements and reproducibility. To address these challenges, a high-throughput image analysis-based method has been developed to evaluate the filterability of precipitated biomolecules, with mRNA serving as a model system. Morphological features extracted from visual data, including precipitate size and distribution, enable rapid screening of precipitation conditions, achieving up to a 90 % reduction in material consumption compared to conventional methods. This approach facilitates the identification of optimal salts and additives to improve precipitation efficiency and downstream recovery, supporting the advancement of scalable precipitation-based capture strategies within integrated continuous biomanufacturing.

1. Introduction

In recent years, there has been growing interest in non-titer-dependent and non-chromatographic alternatives for the initial capture of high-value therapeutic products within integrated continuous downstream processes. Among these, precipitation has emerged as a particularly promising strategy due to its simplicity, scalability, and compatibility with continuous processing [1–11].

Precipitation relies on reducing the solubility of target molecules to induce their aggregation and subsequent removal from solution. It can be triggered by changes in pH, ionic strength, temperature, or the addition of precipitating agents, offering a cost-effective and scalable solution for the capture of biomolecules [1,5,11–18]. Once the target has been precipitated, an efficient solid-liquid separation step is essential to isolate it from the surrounding liquid phase and enable further processing. For processes where the main product is precipitated, its recovery is typically achieved using tangential flow filtration (TFF). However, continuous operation of TFF presents considerable challenges, particularly in maintaining stable filtration performance over extended periods. A critical parameter in this context is the critical flux, defined as

* Corresponding author.
E-mail address: braatz@mit.edu (R.D. Braatz).

https://doi.org/10.1016/j.seppur.2026.136946
Received 30 November 2025; Received in revised form 14 January 2026; Accepted 16 January 2026
Available online 19 January 2026

the maximum permeate flux at which membrane fouling is negligible [9,19,20], thereby ensuring sustained operational stability. Recent studies have highlighted the crucial role of the three-dimensional structure of precipitates in their recovery and dissolution. For example, Pons Royo et al. [8] demonstrated that the size distribution and density of precipitated monoclonal antibodies (mAbs) are influenced by the mode and duration of the addition of polyethylene glycol (PEG) and consequently its filterability. Minervini et al. [3] showed that factors such as pH, buffers, and salts can significantly influence the properties of the precipitate. Moreover, they found that certain additives can stabilize precipitate structures, resulting in higher packing densities and improved filterability. These observations highlight a strong link between structural order within precipitates and favorable filtration properties, including enhanced critical flux. While these effects have been well-characterized for mAbs, they have not yet been systematically investigated for mRNA. Accurately assessing packing density is therefore key to predicting filterability, yet existing methods present notable drawbacks. Packing density is typically determined using batch centrifugation, where the precipitate is compressed and its mass measured to calculate compactness based on the total mass of the centrifuged pellet. However, this method requires large sample volumes and high concentrations of the target molecule, which can be prohibitive when working with costly materials such as mRNA.

Other conventional techniques for analyzing precipitate structure, such as cryo-transmission electron microscopy and light scattering, are expensive and time-consuming [21]. Consequently, there is still no simple, high-throughput method for reliably assessing filterability.

Considering these limitations, there is a clear need for strategies that allow rapid, reproducible evaluation of precipitate properties while minimizing material consumption. Computational image-based approaches offer a promising solution, enabling high-throughput analysis without the constraints of conventional workflows. In particular, image processing algorithms have found broad application in biotechnology and bioprocess engineering due to their accuracy, robustness, and flexibility across a range of analytical tasks [12]. Image analysis relies on pixel-level algorithms to extract relevant features such as color intensity, object boundaries, and morphological descriptors (e.g., area, shape, eccentricity). These techniques are well-suited for structured, low-complexity tasks, offering high interpretability and ease of implementation. When applied to precipitation studies, they enable the characterization of key precipitate features such as colorimetric properties (hue, saturation, brightness), morphological descriptors (eccentricity), and dimensional estimates (projected area and volume), which can be directly related to important process characteristics like filterability.

Herein, we present a proof-of-concept study demonstrating how salt type and concentration influence mRNA precipitation and the resulting filtration behavior. We employ a high-throughput screening method, integrated with image segmentation, to evaluate the filterability of biomolecules such as mRNA. This approach enables rapid assessment of diverse precipitating agents, facilitating the identification of optimal candidates to enhance the efficiency of precipitation–filtration processes in biopharmaceutical purification while simultaneously reducing time and material costs. Moreover, this strategy could be extended to other biomolecules, including monoclonal antibodies, to systematically optimize precipitation and filtration performance across different therapeutic modalities.

2. Materials and methods

2.1. mRNA crude construct

All experiments used crude Fluc mRNA (1 g/L) obtained from Arranta Bio/Recipharm (USA). Samples were stored at −20 °C for short-term use and −80 °C for long-term preservation.

2.2. Precipitation screenings

For the precipitation screenings, 100 µL of crude IVT mRNA solution was mixed with 100 µL of each solution from the commercial GRAS Screen™ 7 crystallization kit (Hampton Research, USA), which contains 96 distinct salt-based precipitation conditions, in a 96-well U-shaped plate (ThermoFisher, USA). Plates were incubated on a shaker at 750 rpm for 60 min, then centrifuged at 3000 rpm for 15 min using an Eppendorf 5810 centrifuge. After centrifugation, 100 µL of supernatant was collected and transferred to a PCR 96-well plate for further analysis.

2.3. Size exclusion chromatography (SEC)

Precipitation yield of mRNA was assessed using size-exclusion chromatography with a Bio SEC-5 column (5 µm, 4.6 × 150 mm, 2000 Å; Agilent, USA). Analysis was performed on a Dionex Ultimate 3000 HPLC system equipped with a diode array detector (Thermo Fisher Scientific, MA, USA). The mobile phase consisted of 100 mM phosphate buffer at pH 7.0 (Merck KGaA, USA), filtered through 0.22 µm membranes and degassed prior to use. A 1 µL sample volume was injected, and absorbance was monitored at 260 nm. Data were processed using Chromeleon™ software (Thermo Fisher Scientific). Precipitation yield was calculated by comparing the main peak area of the initial sample to that of the supernatant following precipitation.

2.4. Packing density

The packing density of the precipitates was determined by measuring the mass of the pellet obtained after centrifugation. Precipitation was performed using 3 M stock solutions of the selected salts, except for ammonium phosphate, which was used at a concentration of 1.5 M. A final concentration of 0.75 M was applied to crude mRNA samples. Following precipitation, the samples were centrifuged, and the supernatant was carefully discarded. The pellet mass was calculated by subtracting the weight of the empty centrifuge tube from that of the tube containing the wet pellet. Packing density was then evaluated according to the method described by Minervini et al. [3].

2.5. Filterability assessment

The filterability of mRNA precipitates was assessed using constant-flux membrane filtration. The precipitate suspensions were circulated through a hollow fiber module (MicroKros, 20 cm length, 0.2 µm pore size, PES, Repligen, USA) following the procedure described in Pons Royo et al. [22]. The feed flow rate was set to 50 mL min^{-1} using a peristaltic pump (Repligen, USA), while the permeate flux was maintained at a constant 0.25 mL min^{-1} by means of a secondary pump connected to the permeate outlet. Feed, retentate, and permeate pressures were continuously monitored using pressure sensors (Pendotech, USA) throughout the process. Filtration was terminated once a sharp increase in transmembrane pressure (TMP) indicated the onset of significant membrane fouling. After each experiment, the hollow fiber membranes were cleaned with 0.5 M NaOH and thoroughly rinsed with RNase-free water prior to reuse.

2.6. Image acquisition

To evaluate mRNA precipitation across a broad range of conditions, 96-well plates were used. Following centrifugation, the plates were transferred to an Olympus BX63F motorized microscope system equipped with both motorized focus and stage. Imaging was performed using a low-magnification, long-working distance objective (LMPLFLN5×; LWD M Plan FL 5× Objective, NA 0.13, WD 22.5 mm), which provided optimal scanning of the precipitates at the bottom of each well as well as the entire plate. To enhance contrast, transmitted light (12 V/100 W HAL lamp) was used during imaging. Automated image stitching was

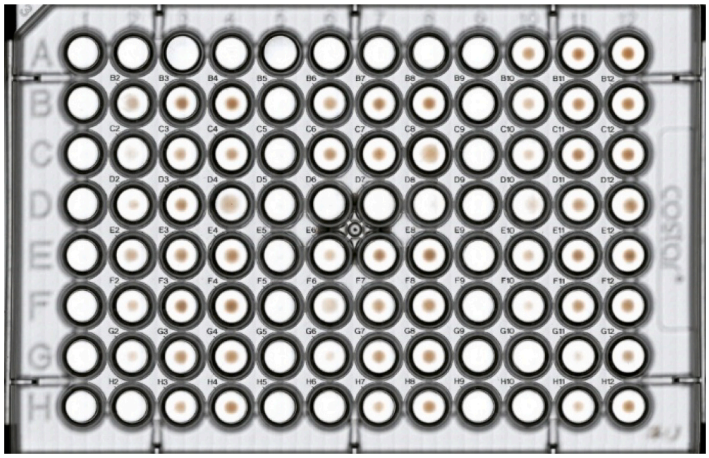

Fig. 1. Overview of the 96-well plate precipitation screening. Each well contained a distinct salt type and concentration to evaluate mRNA precipitation.

carried out within the cellSens Dimension 4.3 software, and the final stitched images were exported for subsequent image analysis (Fig. 1).

2.7. Image segmentation

A quantitative evaluation of precipitate filterability was performed using a multi-stage image processing pipeline. This approach was developed to provide robust and precise segmentation of the precipitate material in each well image, serving as the foundation for subsequent analytical measurements (Fig. 2).

The original Images ($\mathbf{X}_i^{\mathrm{RGB}}$) were converted from the standard RGB (Red-Green-Blue) color space to HSV (Hue-Saturation-Value) to separate color information from brightness ($\mathbf{X}_i^{\mathrm{HSV}}$; for simplicity they will be refered as $\mathbf{X}_i$). This transformation separates chromatic components (Hue and Saturation) from the luminance component (Value), allowing for more consistent color detection based on the intrinsic properties of the precipitate, regardless of illumination differences.

Firstly, a spatial refinement technique was introduced to focus analytical efforts following color space transformation. A circular Region of Interest (ROI) mask was algorithmically defined. For each input image $\mathbf{X}_i$ (with width W_i and height H_i), a circular binary mask $\mathbf{M}_i \in \{0,1\}^{H_i \times W_i}$ was generated. The center of the image was determined as

$$\boldsymbol{c}_i = \left(c_{ix}, c_{iy}\right)^{\mathrm{T}} = \left(\frac{W_i}{2}, \frac{H_i}{2}\right)^{\mathrm{T}}$$

The circular well is detected automatically using the plate radius r. The analysis ROI is defined as Θr centered at c_i, thereby restricting processing to the inner well region where precipitate is typically observed. An empirically value $\Theta = 0.9$ was adopted to all images to capture the complete precipitate while reducing computational cost. Then, for each pixel at coordinates $\mathbf{p} = \left(p_x, p_y\right)^{\mathrm{T}}$ in the image $\mathbf{X}_i$, the corresponding value in the mask $\mathbf{M}_i$ is defined as

$$\mathbf{M}_i(\mathbf{p}) = \begin{cases} 1, \text{if } \|\mathbf{p} - \mathbf{c}_i\|_2^2 \leq (\Theta r)^2 \\ 0, \text{otherwise} \end{cases}$$

Processing is restricted to this ROI, which covers the central area where the precipitate is typically present. By confining analysis to this region, computation is reduced and accuracy is improved. A binary mask is then defined: each pixel inside the ROI is assigned value 1; all other pixels are assigned 0.

The core segmentation stage was executed with the image data prepared and spatially focused. This involved applying a particular color threshold within the HSV domain, established through a semi-automatical calibration. A small, stratified subset of representative wells (15 wells covering salts and low/medium/high contrast) was used to tune the HSV bounds. For this subset, reference precipitate masks were defined to ensure that the precipitate region was fully covered and background spill inside the ROI was visually negligible. A coarse-to-fine grid search was then run over the HSV bounds, and the parameters that maximized the mean Dice similarity index against the reference masks were selected, breaking ties by shorter boundary length (smoother contours). The selected parameters were subsequently frozen and applied unchanged to held-out batches; no further edits were made. The unique HSV signature accurately characterizing the precipitate were: hue values within 1 and 25; Saturation within 1 and 200; Value within 100 and 255. Pixels whose HSV values fell within this defined range were classified as belonging to the precipitate, generating an initial binary mask ($B_i^{(1)}$).

While capturing the bulk of the precipitate, $B_i^{(1)}$ could occasionally include minor spurious artefacts or discontinuities. The binary mask was regularized by an opening followed by a closing operation. A fixed kernel was used because all images were acquired with the same camera, optics, and resolution, so a fixed number of pixels corresponds to the same physical scale across the dataset. The disk shape was chosen to respect the circular symmetry of the wells and to avoid orientation bias from square elements. This operation was introduced to remove small speckles and fill pin-holes caused by sensor noise and local illumination, while preserving the precipitate contour. Formally, the morphological *opening* operation (erosion followed by dilation) systematically eliminated small, isolated pixel clusters and smoothed object outlines:

$$B_i^{(2)} = \left(B_i^{(1)} \ominus \mathbf{K}\right) \oplus \mathbf{K},$$

where $\ominus$ refers to the erosion operation, $\oplus$ to the dilation operation, and $\mathbf{K}$ is the structuring element corresponding to a 3×3 all-ones matrix. Subsequently, a morphological *closing* operation (dilation followed by erosion) filled small internal holes within segmented regions:

$$B_i^{(3)} = \left(B_i^{(2)} \oplus \mathbf{K}\right) \ominus \mathbf{K}.$$

Across plates, this morphology step produced only minor changes in measured area and did not alter the direction or significance of any reported association.

The final stage of the segmentation pipeline involved a contour-based object selection protocol. After morphological refinements, all distinct, contiguous regions (contours) within the binary mask were identified and their areas calculated. A selection criterion based on a minimum permissible area was applied, defined as

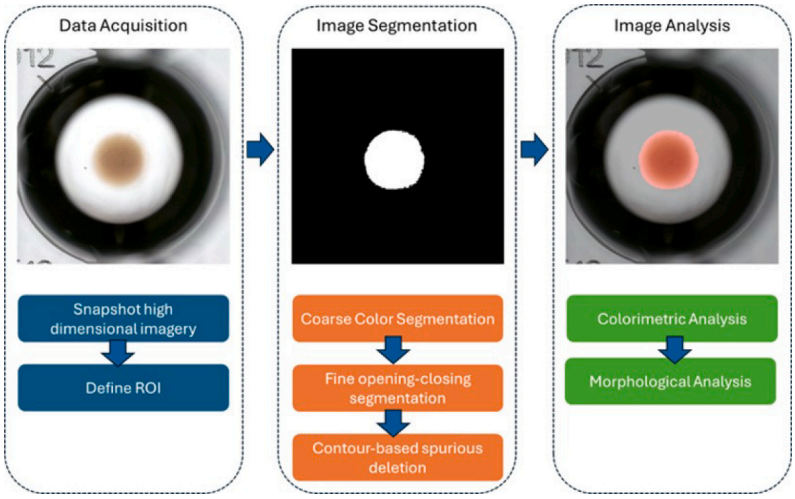

Fig. 2. Image segmentation flow diagram. (A) Original well image. (B) Segmentation mask generated by the processing pipeline. (C) Mask overlaid on the well image, used for all mathematical analyses.

$$B^{\text{final}}(\mathbf{p}) = \begin{cases} 1, \text{for } \mathbf{p} \in \underset{j:|C_j| \geq \alpha W_i H_i}{\text{argmax}} |C_j| \\ 0, \text{otherwise} \end{cases}$$

where C_j is the set of detected contours in the image, the operator $|.|$ is the total number of pixels of the contour, and α is the minimum percentage permitted of the total image (fixed to a 0.1 value). This step allowed for automatically discarding any remaining minor, non-representative artefacts. The largest contour meeting this criterion was designated as the definitive segmentation.

2.8. Image analysis

After the segmentation process, each identified precipitate was characterized quantitatively, focusing on its (I) colorimetric, (II) morphological, and (III) dimensional attributes.

1. The colorimetric properties of the precipitate were assessed by analyzing the distribution of pixel values within the segmented region in the HSV color space. The mean, median, and standard deviation were computed from the population of pixels constituting the precipitate for each of the H, S, and V channels. These metrics provide a quantitative summary of the central tendency (e.g., average color tone), dispersion (e.g., color uniformity), and the most frequent color characteristics of the material. Saturation values are especially relevant as they contain information on the precipitation intensity.
2. Morphological analysis focused on the shape of the segmented precipitate. It can be characterized by its eccentricity. This parameter is determined by fitting an equivalent ellipse to the main contour of the segmented region (using the least-squares method) [23]. Eccentricity quantifies the precipitate's elongation, providing a measure of its deviation from a perfectly circular form. A value of 0 indicates a circle, and values approaching 1 indicate an increasingly elongated shape.
3. Dimensional attributes included the projected area and an estimated volume of the precipitate. The projected pixel area A_p was first determined directly from the segmented mask. This pixel-based area was then converted to a real-world area A_r (in mm^2) using a calibrated scaling factor derived from system optics, corresponding to 6.86 mm for every 2120 pixels. Subsequently, an estimated volume V (in mm^3) was calculated. The well bottom (where the particles precipitate) follows a convex curvature. The volume computation assumes that the measured projected area A_r corresponds to the circular base of a spherical cap, which itself is part of a larger sphere with a known radius $R_{\text{sphere}} = 3.22$ mm. From A_r, the radius of the cap's base was calculated as $r_{\text{base}} = \sqrt{\frac{A_r}{\pi}}$. The height h of the spherical cap, representing the effective depth of the precipitate, was determined using the relationship $h_{\text{cap}} = R_{\text{sphere}} - \sqrt{\left(R_{\text{sphere}}^2 - r_{\text{base}}^2\right)}$. Finally, the volume of the precipitate V, defined by the spherical cap, was calculated using the standard formula:

$$V = \frac{1}{3}\pi h_{\text{cap}}^2 \left(3R_{\text{sphere}} - h_{\text{cap}}\right).$$

3. Results and discussion

3.1. Image analysis

To evaluate the impact of salt type on mRNA precipitate formation, 96 distinct salt-based precipitation conditions were screened. Quantitative image analysis was subsequently employed to characterize precipitate morphology, distribution, and intensity. U-shaped plates were chosen because their curved bottoms allow precipitate to settle centrally, enabling clear differentiation and accurate morphological analysis. In contrast, other plate types can result in uneven or overly concentrated precipitate, making imaging and morphological assessment unfeasible. This approach provided a quantitative and consistent characterization of precipitate formation across all simples.

In this section, two illustrative examples are given, one containing a visually intense precipitate formation (Fig. 3a), and one exhibiting a weak formation (Fig. 3b). The contour is shown in green surrounding the precipitate.

The capability of the system to differentiate precipitate characteristics is demonstrated through a comparative analysis of samples with visually distinct formation intensities. Intense precipitates are shown in the left panels of Figs. 5, 6 and 7, while weak precipitates appear in the corresponding right panels. Colorimetric analysis in the HSV color space highlighted both key differences and similarities between these samples. In the Hue channel, both intense (Fig. 4a) and weak (Fig. 4b) precipitates exhibited hues predominantly within the orange-to-brown range. Their distributions peaked within a similar range (H values approximately 15 to 30 on a 0 to 179 scale), indicating that the fundamental base color signature of the precipitate remained largely consistent regardless of intensity or quantity.

The Saturation channel served as a key differentiator between precipitate intensities. Intensely formed precipitates (Fig. 5a) exhibited a broad distribution with a substantial proportion of pixels displaying

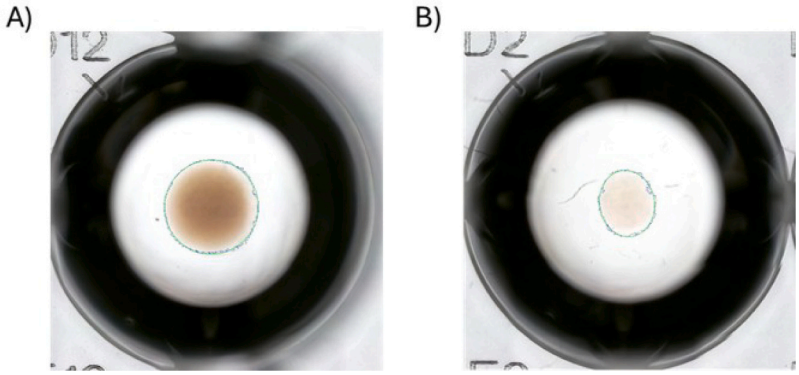

Fig. 3. Representative images of precipitate formation with the precipitate regions outlined in green. (a) Intense precipitate formation. (b) Weak precipitate formation. (For interpretation of the references to color in this figure legend, the reader is referred to the web version of this article.)

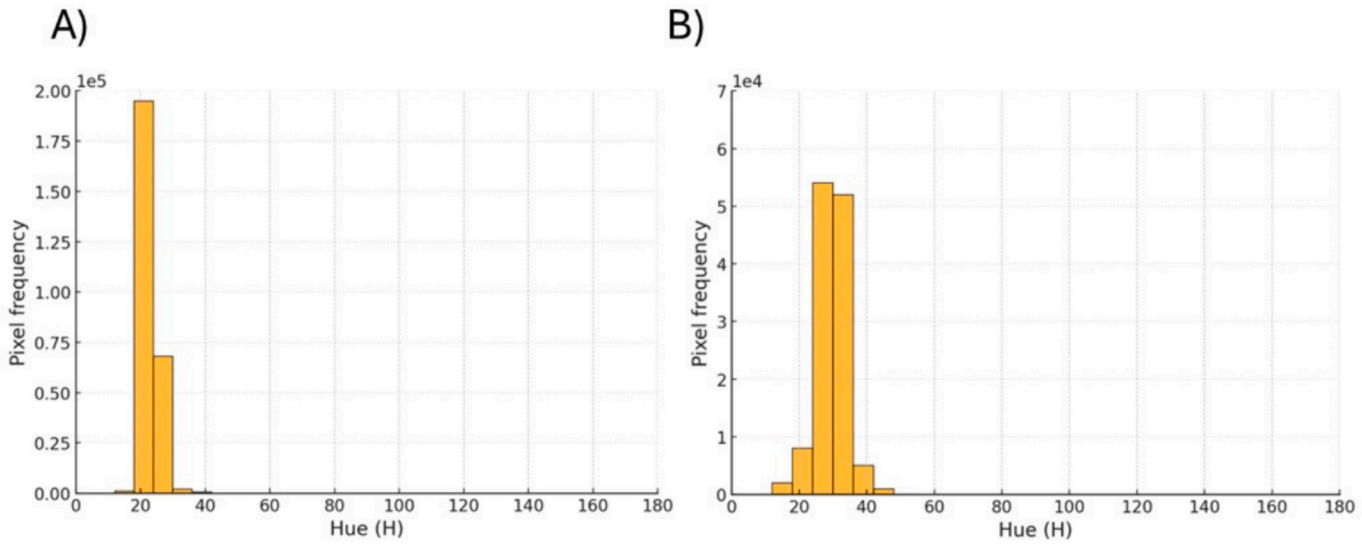

Fig. 4. Representative images illustrating precipitate formation with hue analysis. (a) Intense precipitate formation exhibiting hues predominantly in the orange-to-brown range. (b) Weak precipitate formation showing a similar hue distribution. (For interpretation of the references to color in this figure legend, the reader is referred to the web version of this article.)

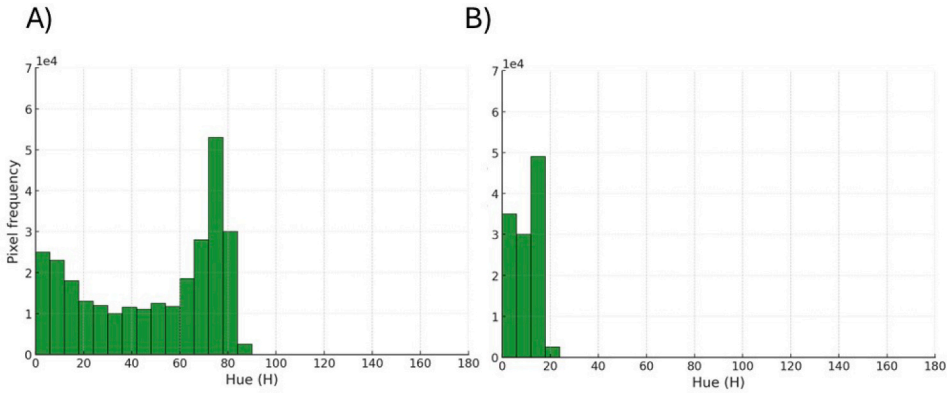

Fig. 5. Representative images illustrating precipitate formation with saturation analysis. (a) Intense precipitate formation exhibiting high saturated colors. (b) Weak precipitate formation showing low saturated colors.

high saturation values (often $S > 100$), indicating a vivid, rich, and well-defined coloration. In contrast, weak precipitates (Fig. 5b) showed saturation values predominantly clustered in the lower range (e.g., $S < 50$), reflecting a desaturated, more diffuse, or pale appearance with a less distinct chromatic presence.

Similarly, the Value channel, which represents brightness, revealed notable differences between precipitate types. Intense precipitates (Fig. 6a) exhibited a broad distribution skewed toward higher Value pixels (e.g., many pixels with $V > 150$), indicating a bright and opaque material. In contrast, weak precipitates (Fig. 6b) also contained highly

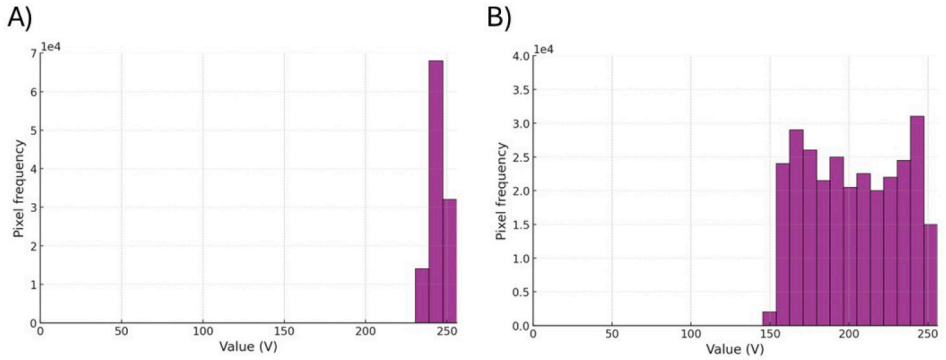

Fig. 6. Representative images illustrating precipitate formation with value analysis. (a) Intense precipitate formation exhibiting a spread distribution of values from 150 to 255. (b) Weak precipitate formation showing narrower distributions close to 250.

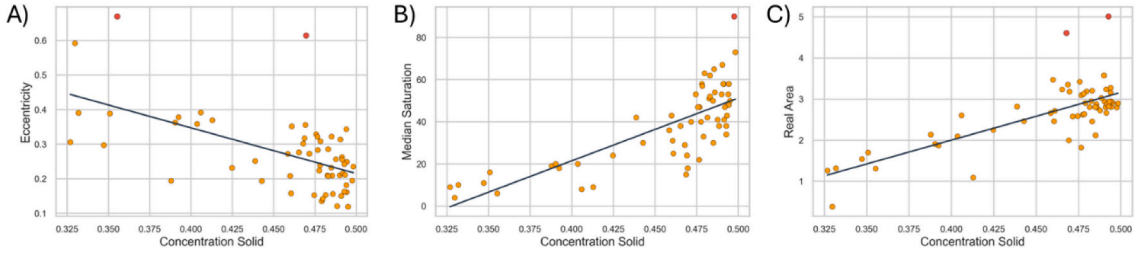

Fig. 7. Correlation of precipitate properties with solid concentration. Scatter plots depicting the relationship between solid concentration and (A) eccentricity, (B) median saturation, and (C) real area of precipitates. Each point represents an individual measurement, and linear regression lines indicate overall trends. Outliers are highlighted in red to distinguish them from the main dataset. (For interpretation of the references to color in this figure legend, the reader is referred to the web version of this article.)

luminous pixels but displayed a narrower distribution, often sharply concentrated near the upper limit of the value scale. This suggests that although individual particles in the weak precipitate are bright, their overall presence is less substantial, potentially more dispersed, and contributes to a less uniformly opaque appearance.

Further analysis of the complete dataset, incorporating known solid concentrations (g/L) for each sample, revealed statistically significant correlations between this key process parameter and the image-derived precipitate characteristics (Table 1). A strong positive correlation (Pearson's $r = 0.73$, $p < 0.001$) was observed between the solid concentration and the measured precipitate area, indicating that higher concentrations generally result in larger projected precipitate regions. Similarly, a strong positive correlation (Pearson's $r = 0.76$, $p < 0.001$) was identified between solid concentration and overall color intensity (as captured by saturation and value metrics), suggesting that precipitates formed at higher concentrations tend to display more pronounced and vivid color characteristics. Furthermore, a moderate negative correlation (Pearson's $r = -0.57$, $p < 0.001$) emerged between solid concentration and precipitate eccentricity. This finding implies that higher solid concentrations are associated with the formation of precipitates that are more regular and circular in shape (i.e., less eccentric). Pairwise relationships with density were visualized using regression plots (Fig. 7), with regression curves overlaid on the data points. Outliers are highlighted in red and correspond to wells A12 (saturation), C8 and D4 (area), and B2 and C2 (eccentricity). Excluding these wells had negligible effects on effect sizes and statistical significance, and rank-based estimates (Spearman correlations) remained similar. These results indicate that the reported associations are robust to outliers and slight deviations from linearity.

Table 1
Pearson's correlation values for image analysis.

	Color (median of saturation)	Eccentricity	Area (mm^2)	Density ($\frac{g}{L}$)
Color (median of saturation)	1	−0.60	0.56	0.76
Eccentricity		1	−0.46	−0.57
Area			1	0.73
Density				1

The intercorrelations among the image-derived features themselves were consistent with these primary findings. For instance, a moderate negative correlation was observed between precipitate area and eccentricity (Pearson's $r = -0.46$, $p < 0.001$), and a notable negative correlation between color intensity and eccentricity (Pearson's $r = -0.60$, $p < 0.001$), further suggesting that more substantial and intensely colored precipitates tend toward more circular forms. The extremely low p-values associated with all reported correlations indicate a statistical significance, implying that these observed relationships are improbable due to random chance. The comprehensive list of results, including the raw images and segmentation masks has been made available in an online repository to facilitate further exploration.[1]

3.2. Selection of salts for further evaluation

Formation of mRNA precipitates was systematically evaluated across a variety of salts using image analysis techniques. Key parameters analyzed included precipitate area and median saturation, which served as indicators of the precipitate's morphology and packing density, respectively. The analysis revealed that the nature of the salt strongly influenced precipitation behavior, with certain salts yielding significantly smaller and denser precipitates compared to others. Moreover, increasing the salt concentration generally resulted in higher packing densities and smaller precipitate sizes for the same salt type. However,

[1] https://mateocamara.github.io/wells_analysis/

higher concentrations can also promote the undesirable coprecipitation of impurities, potentially affecting downstream purification processes. To account for this, all measured values were normalized by the corresponding salt concentration to enable an unbiased comparison of salt performance. A performance coefficient was then defined as (precipitate area × median saturation) divided by the salt concentration. This coefficient provided an integrated metric reflecting both the size and compactness of the precipitates relative to salt concentration. Salts with higher coefficients were considered to have superior precipitation characteristics, while those with lower coefficients were deemed less effective. Among the tested salts, ammonium phosphate and potassium phosphate consistently exhibited the lowest coefficient values, indicating larger or less compact precipitates, even at elevated concentrations. In contrast, salts such as ammonium tartrate and ammonium sulfate showed high coefficients, corresponding to the formation of smaller, denser precipitates, which are generally preferred for efficient purification. Based on these findings and considering salt availability, two representative salts from the best-performing and worst-performing groups were selected for more detailed investigation (Table 2).

These results demonstrate that both the type and concentration of salts significantly influence the morphology and packing density of mRNA precipitates, and consequently their filterability. Similar salt-dependent effects have been observed previously for monoclonal antibodies (mAbs), highlighting a common mechanistic role of salts in biomolecular precipitation. Image analysis provided an effective high-throughput platform for screening and characterization, enabling quantitative assessment of precipitate size, shape, and colorimetric features. While these measurements offer valuable comparative insights, understanding the mechanisms underlying the observed variations is essential for the rational optimization of precipitation processes. The observed improvements in filterability were not solely due to changes in particle size distribution but were primarily driven by increased precipitate compactness and enhanced internal structural order [3,24]. It should be noted that this study focuses exclusively on solution parameters, including salt type and buffer composition, without accounting for hydrodynamic effects such as mixing intensity or shear, which can also influence precipitate structure and downstream filtration performance [25–27].

A key determinant of salt performance is their position in the Hofmeister series [28,29], which classifies ions based on their ability to promote macromolecular precipitation. Kosmotropic salts, such as ammonium sulfate, ranked among the top-performing agents in our study. These ions stabilize the structure of water and preferentially exclude solutes, enhancing macromolecular interactions and favoring the formation of denser, more compact aggregates [28,29]. This effect explains the high packing density and superior filterability observed with ammonium sulfate and citrate-based systems. In contrast, salts such as ammonium phosphate and potassium phosphate exhibited significantly poorer performance in both image-based morphology assessments and filtration tests. Although they are generally considered strong kosmotropic salts, their poor performance suggests that other, more specific interactions may be influencing the precipitation behavior [28,29]. This discrepancy indicates that salt-induced precipitation is governed not only by general Hofmeister effects but also by specific ion-macromolecule interactions [30,31]. In the case of phosphate-containing salts, the strong negative charge of phosphate ions may lead to electrostatic repulsion with the negatively charged phosphate backbone of RNA [30]. Such unfavorable interactions can disrupt uniform aggregation, resulting in looser and less compact precipitates that tend to foul filtration membranes more rapidly, as indicated by sharp increases in transmembrane pressure. Overall, our results underscore the importance of considering both classical ion-ranking frameworks and specific ion-biomolecule interactions when selecting salts for RNA precipitation. This dual perspective is critical for the development of more efficient and scalable purification strategies.

Table 2
Classification of salts based on precipitation performance.*

Best performing		Worst performing	
Ammonium tartrate	93.69	Sodium acetate	57.89
Ammonium sulfate	**93.11**	Ammonium formate	54.09
Ammonium citrate tribasic	**77.34**	**Ammonium phosphate**	**30.22**
Ammonium acetate	73.59	**Potassium phosphate**	**24.96**
Ammonium chloride	60.46	–	–

* In bold, the selected salts.

3.3. Packing density and filterability assessment

To validate the salt classification derived from image segmentation and to investigate differences in precipitate behavior, the packing density of mRNA precipitates formed using selected salts (Table 2) was measured (Table 3). Precipitates were prepared at a fixed mRNA concentration of 1 g/L in a final concentration of 0.75 M salt solutions to ensure consistency across all experiments. Ammonium sulfate produced the highest packing density (16.52 ± 4.80), followed by ammonium citrate (13.43 ± 0.80). In contrast, ammonium phosphate (8.15 ± 1.51) and potassium phosphate (8.84 ± 1.43) exhibited significantly lower packing densities. These trends are consistent with the image analysis data, which indicated denser and more uniform precipitate structures for ammonium sulfate and ammonium citrate compared to the looser, more heterogeneous precipitates formed with ammonium phosphate and potassium phosphate.

To further characterize functional differences among the precipitates, filterability was evaluated by monitoring TMP) during membrane filtration of mRNA precipitates formed with the selected salts (Table 2 and Fig. 8). The TMP profiles revealed distinct fouling behaviors. Precipitates formed with ammonium phosphate and potassium phosphate caused rapid increases in TMP, exceeding 6 psi within minutes, indicating poor filterability and significant membrane fouling. In contrast, precipitates formed with ammonium citrate and ammonium sulfate maintained low and stable TMP values throughout the 40-min filtration period, demonstrating superior filterability and minimal fouling. These filtration results are consistent with the differences observed in packing density.

The analysis confirms that the image-based approach effectively identifies salts that produce precipitates with higher packing densities, which correlate with improved filterability and higher critical flux values. Notably, this method requires only 100 µL of sample per condition, corresponding to a 90 % reduction in volume compared with the minimum 1 mL needed for conventional packing density measurements, thereby enabling more efficient material use. This high-throughput setup facilitates the rapid evaluation of multiple salts and precipitation conditions, offering valuable insights into optimal process parameters. By automating the analysis, a broader range of experimental conditions can be screened in substantially less time, while minimizing operator-related variability. Overall, this strategy enhances both the efficiency and reliability of early-stage screening and contributes to a deeper understanding of salt effects on particle formation. Importantly, the same image-based approach could be applied to other biomolecules, such as monoclonal antibodies, providing a versatile platform to systematically optimize precipitation and filtration performance across different therapeutic proteins.

Table 3
Packing density of mRNA precipitates formed using different salts.

Salt	mRNA – Packing density
Ammonium Sulfate	16.52 ± 4.80
Ammonium citrate	13.43 ± 0.80
Ammonium phosphate	8.15 ± 1.51
Potassium phosphate	8.84 ± 1.43

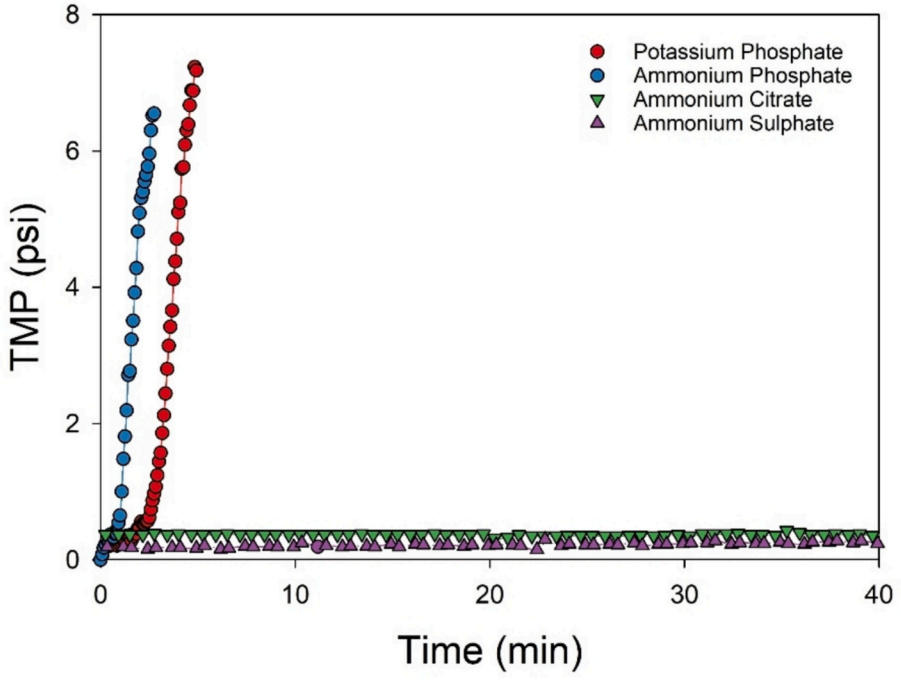

Fig. 8. Transmembrane pressure profiles during membrane filtration of mRNA precipitates formed with different salts.

4. Conclusion

In this study, we systematically investigated for the first time how salt type influences mRNA precipitation and the resulting filterability of the precipitates. We demonstrated a proof-of-concept high-throughput screening method, integrated with rapid image segmentation, to evaluate precipitate filterability of biomolecules. The developed segmentation algorithm showed consistent performance and very good reproducibility compared to conventional techniques such as manual packing density determination. The use of algorithm for image analysis offers several advantages, including reduced reagent and sample consumption, shorter experimental times through streamlined workflows, and increased high-throughput capacity. By automating the analysis of precipitate filterability, a much broader range of experimental conditions can be efficiently screened while minimizing human-related variability such as operator bias. This image analysis driven approach enables rapid and systematic evaluation of precipitating agents, accelerating the identification of optimal candidates to enhance the efficiency of precipitation-filtration steps in biopharmaceutical purification, while reducing both time and costs.

Declaration of competing interest

The authors declare that they have no known competing financial interests or personal relationships that could have appeared to influence the work reported in this paper.

Acknowledgements

This research was funded by the U.S. Food and Drug Administration through the FDA BAA-22-00123 program, under Award Number 75F40122C00200.

Data availability

Data will be made available on request.

References

[1] Y. Zhu, M. Mergy, S.M. Cramer, T.M. Przybycien, Towards platformization of monoclonal antibody capture precipitation solution conditions in the PEG-zinc precipitant system, Sep. Purif. Technol. 361 (2025) 131138.
[2] M. Minervini, M. Mergy, Y. Zhu, M.A. Gutierrez Diaz, C. Pointer, O. Shinkazh, S. F. Oppenheim, S.M. Cramer, T.M. Przybycien, A.L. Zydney, Continuous precipitation-filtration process for initial capture of a monoclonal antibody product using a four-stage countercurrent hollow fiber membrane washing step, Biotechnol. Bioeng. 121 (2024) 2258–2268.
[3] M. Minervini, A. Behboudi, J.R. Marzella, A.L. Zydney, Optimizing particle morphology during antibody precipitation for enhanced tangential flow filtration performance, Sep. Purif. Technol. 338 (2024) 126574.
[4] X. Feng, Z. Li, Z. Su, S. Che, B. Dai, Y. Cheng, S. Zhang, Rapid and high recovery isolation of mRNA from in vitro transcription system by ammonium sulphate precipitation at room temperature, Sep. Purif. Technol. 336 (2024) 126331.
[5] M.D.C. Pons Royo, T. De Santis, D. Komuczki, P. Satzer, A. Jungbauer, Continuous precipitation of antibodies by feeding of solid polyethylene glycol, Sep. Purif. Technol. 304 (2023) 122373.
[6] D. Ferreira-Faria, F. Domingos-Moreira, M.R. Aires-Barros, A. Ferreira, A. M. Azevedo, Continuous precipitation of antibodies using oscillatory flow reactor: a proof of concept, Sep. Purif. Technol. 317 (2023) 123924.
[7] M.D.C. Pons Royo, J.-L. Beulay, E. Valery, A. Jungbauer, P. Satzer, Design of millidevices to expedite apparent solubility measurements, React. Chem. Eng. 7 (2022) 2045–2053.
[8] M.D.C. Pons Royo, J.-L. Beulay, E. Valery, A. Jungbauer, P. Satzer, Mode and dosage time in polyethylene glycol precipitation process influences protein precipitate size and filterability, Process Biochem. 114 (2022) 77–85.
[9] Z. Li, T.-H. Chen, E. Andini, J.L. Coffman, T. Przybycien, A.L. Zydney, Enhanced filtration performance using feed-and-bleed configuration for purification of antibody precipitates, Biotechnol. Prog. 37 (2021) e3082.
[10] G. Recanati, M. Pappenreiter, C. Gstoettner, P. Scheidl, E.D. Vega, B. Sissolak, A. Jungbauer, Integration of a perfusion reactor and continuous precipitation in an entirely membrane-based process for antibody capture, Eng. Life Sci. 23 (2023) e2300219.
[11] N. Hammerschmidt, S. Hobiger, A. Jungbauer, Continuous polyethylene glycol precipitation of recombinant antibodies: sequential precipitation and resolubilization, Process Biochem. 51 (2016) 325–332.
[12] D. Burgstaller, A. Jungbauer, P. Satzer, Continuous integrated antibody precipitation with two-stage tangential flow microfiltration enables constant mass flow, Biotechnol. Bioeng. 116 (2019) 1053–1065.
[13] N. Hammerschmidt, B. Hintersteiner, N. Lingg, A. Jungbauer, Continuous precipitation of IgG from CHO cell culture supernatant in a tubular reactor, Biotechnol. J. 10 (2015) 1196–1205.
[14] N. Lingg, M. Mozgovicz, T. Schaufler, A. Prokup, A. Carruthers, D. Boerema, L. Keigher, N. Brinkman, A. Jungbauer, Continuous cold ethanol precipitation of immunoglobulin G from human plasma, Process Biochem. 132 (2023) 121–129.

[15] N. Hillebrandt, P. Vormittag, N. Bluthardt, A. Dietrich, J. Hubbuch, Integrated process for capture and purification of virus-like particles: enhancing process performance by cross-flow filtration, Front. Bioeng. Biotechnol. 8 (2020).
[16] A. Dietrich, R. Schiemer, J. Kurmann, S. Zhang, J. Hubbuch, Raman-based PAT for VLP precipitation: systematic data diversification and preprocessing pipeline identification, Front. Bioeng. Biotechnol. 12 (2024).
[17] M.D.C. Pons Royo, T. Arnold, I. Perez Rodriguez, N. Ostrovsky, M. Al-Jazrawe, A. Hatas, V. Tenberg, A.S. Myerson, R.D. Braatz, Purification of messenger RNA directly from crude IVT using polyethylene glycol and NaCl precipitation, Process Biochem. 156 (2025) 263–273.
[18] N. Hammerschmidt, A. Tscheliessnig, R. Sommer, B. Helk, A. Jungbauer, Economics of recombinant antibody production processes at various scales: industry-standard compared to continuous precipitation, Biotechnol. J. 9 (2014) 766–775.
[19] Z. Li, A.L. Zydney, Effect of zinc chloride and PEG concentrations on the critical flux during tangential flow microfiltration of BSA precipitates, Biotechnol. Prog. 33 (2017) 1561–1567.
[20] M. Minervini, M. Mergy, Y. Zhu, M. Diaz, C. Pointer, O. Shinkazh, S. Oppenheim, S. Cramer, T. Przybycien, A. Zydney, Continuous precipitation-filtration process for initial capture of a monoclonal antibody product using a four-stage countercurrent hollow fiber membrane washing step, Biotechnol. Bioeng. 121 (2023).
[21] P. Satzer, D. Burgstaller, W. Krepper, A. Jungbauer, Fractal dimension of antibody-PEG precipitate: light microscopy for the reconstruction of 3D precipitate structures, Eng. Life Sci. 20 (2020) 67–78.
[22] M.D.C. Pons Royo, T. Arnold, I.P. Rodriguez, N. Ostrovsky, M. Al-Jazrawe, A. Hatas, A.S. Myerson, R.D. Braatz, Continuous purification of mRNA by precipitation and sequential TFF, Sep. Purif. Technol. 379 (2025) 134837.
[23] R. Halír, J. Flusser, Numerically stable direct least squares fitting of ellipses, in: Proceedings of the 6th International Conference in Central Europe on Computer Graphics, Visualization and Interactive Digital Media (WSCG), 1998, pp. 125–132.
[24] A. Behboudi, M. Minervini, Z.S. Badinger, W.W. Haddad, A.L. Zydney, Addition of sodium malonate alters the morphology and increases the critical flux during tangential flow filtration of precipitated immunoglobulins, Protein Sci. 33 (2024) e5010.
[25] M.D.C. Pons Royo, I. Montes-Serrano, E. Valery, A. Jungbauer, P. Satzer, Milliscale reactors for integration of continuous precipitation and filtration, J. Chem. Technol. Biotechnol. 97 (2022) 3183–3192.
[26] M. Martinez, G. Mannall, M. Spitali, E.L. Norrant, D.G. Bracewell, Reactor design for continuous monoclonal antibody precipitation based upon micro-mixing, J. Chem. Technol. Biotechnol. 97 (2022) 2434–2447.
[27] G. Espuny Garcia del Real, J. Davies, D.G. Bracewell, Scale-down characterization of post-centrifuge flocculation processes for high-throughput process development, Biotechnol. Bioeng. 111 (2014) 2486–2498.
[28] F. Hofmeister, Zur Lehre von der Wirkung der Salze, Arch. Exp. Pathol. Pharmakol. 24 (1888) 247–260.
[29] P. Lo Nostro, B.W. Ninham, Hofmeister phenomena: an update on ion specificity in biology, Chem. Rev. 112 (2012) 2286–2322.
[30] S. Cruz-León, N. Schwierz, Hofmeister series for metal-cation–RNA interactions: the interplay of binding affinity and exchange kinetics, Langmuir 36 (2020) 5979–5989.
[31] K.D. Collins, Ions from the Hofmeister series and osmolytes: effects on proteins in solution and in the crystallization process, Methods 34 (2004) 300–311.